Downdrift Port Siltation Adjacent to a River Mouth: Mechanisms and Effects of Littoral Sediment Transport to the Navigation Channel

Andhy Romdani[1]; Jia-Lin Chen[2]; Hwa Chien[3]; Jing-Hua Lin[4]; Chuan-Kai Hung[5]; and Yu-Qi Huang[6]

Abstract: The mechanisms controlling sediment transport at river mouths and estuaries nearby ports are complicated interactions among waves, tidal currents, and river flows over complex bathymetry. Episodic river discharge triggered by large rainfall may contribute to significant sediment into the ocean. Over the last decade, the exposed riverine sediment from the Zhuoshui River, north of Mailiao Port, is one of the major sources of sediment supply in this region. Previous field observations shortly after the passage of a typhoon suggested fine-grained sediments settled rapidly near the river mouth, and tidal currents and strong wind-driven waves during winter were the mechanisms that transported sediment toward the navigational channel. Numerical simulations provide insights into the patterns of residual circulations for a range of spring-neap tidal forces and wave conditions. Model results show that extending North Jetty could be one of the engineering countermeasures to modify the circulation system between the port and the river mouth to mitigate the siltation problem.
DOI: 10.1061/(ASCE)WW.1943-5460.0000700.

Author keywords: Siltation in waterways; Sediment transport; Navigation improvements; Sedimentation.

Introduction

Ports are crucial connections between sea and land transport and are important to economic development support. Most of the ports worldwide are located in estuarine areas influenced by complex interactions among waves, tidal currents, river flows, and heterogeneous bathymetry. Siltation in navigation channels is a classic problem in port management, and the amount of siltation is directly associated with environmental conditions, morphological configurations, and human behaviors. Dredging is one type of maintenance to reduce siltation; however, port dredging has resulted in high operating costs and potentially negative environmental impacts. A more sustainable method is necessary to reduce sediment transport in ports and to make channel maintenance more efficient.

Previous studies have focused on hydrodynamics and sediment transport in ports and navigation channels. In the Botlek Harbor, within the Port of Rotterdam, salinity-induced density gradients trapped suspended particulate matter (SPM) near the head of the saline water intrusion, determined the availability of SPM exchange between the tidal river and harbor, and caused high siltation rates in the harbor (Nijs et al. 2009). In the Port of Götenborg in Sweden, extensive anthropogenic activities, such as ship traffic and dredging, changed the natural harbor depth and disturbed salinity stratification and patterns of sediment transport (Johannesson et al. 2000). The study based on an experiment of a physical model between the Meuse River and a yacht harbor in Roermond City, the Netherlands, showed that siltation could be substantially reduced through designing a sill in the entrance and a permeable pile-groyne upstream of the entrance (Schijndel and Kranenburg 1998). More recently, studies using numerical models have become more popular because they overcome scaling difficulties in large-scale physical modeling systems as in the case of SPM and sediment transport in the sea near Daishan Island, Zhejiang Province, China (Li et al. 2019). Prumm and Iglesias (2016) investigated the morphodynamic response of the estuary to the expansion of the Port of Ribadeo, Spain, by simulating the impact of port expansion under representative conditions. Results highlighted the significant morphodynamic changes on the eastern bank of the estuary including migration of the tidal delta and infilling of the southeastern and eastern channels. A fully calibrated three-dimensional hydrodynamic model of the Sydney Harbor was used to determine the dominant force of regulating estuarine circulations in the channel under conditions of low river discharge. Modeling studies of the Sydney Harbor revealed that the highly variable cross-channel bathymetry may cause intratidal asymmetries in along estuarine circulations (Xiao et al. 2019). In the present research, a diagnostic study combining field and numerical methods improves understanding of observed downdrift port siltation adjacent to the river mouth. Model results calibrated with observed surface elevations and current velocities provide insights into residual circulations for a range of spring-neap tidal forces and wave conditions over the complex bathymetry.

The study site is located in the central-southern portion of the Taiwan Strait, a transitional zone between the East China Sea and the South China Sea. The mean width of the strait is

---

[1] Dept. of Hydraulic and Ocean Engineering, National Cheng Kung Univ., Tainan City 701, Taiwan; Dept. of Civil Engineering, Siliwangi Univ., Tasikmalaya City 46115, Indonesia. Email: andhy.romdani1925@gmail.com

[2] Dept. of Hydraulic and Ocean Engineering, National Cheng Kung Univ., Tainan City 701, Taiwan (corresponding author). ORCID: https://orcid.org/0000-0002-0084-8832. Email: jialinchenps@gs.ncku.edu.tw

[3] Institute of Hydrological and Oceanic Sciences, National Central Univ., Jhongli City 320, Taiwan. Email: hchien@ncu.edu.tw

[4] Tainan Hydraulics Laboratory, National Cheng Kung Univ., Tainan City 70955, Taiwan. Email: ljh0514@thl.ncku.edu.tw

[5] Dept. of Hydraulic and Ocean Engineering, National Cheng Kung Univ., Tainan City 701, Taiwan. Email: s97807850131@gmail.com

[6] Dept. of Hydraulic and Ocean Engineering, National Cheng Kung Univ., Tainan City 701, Taiwan. Email: x8223195@gmail.com

Note. This manuscript was submitted on November 18, 2020; approved on November 7, 2021; published online on January 13, 2022. Discussion period open until June 13, 2022; separate discussions must be submitted for individual papers. This paper is part of the ***Journal of Waterway, Port, Coastal, and Ocean Engineering***, © ASCE, ISSN 0733-950X.

approximately 180 km. Tidal waves surge into the strait and cause high velocities (Jan et al. 2002; Yu et al. 2017). Exposed riverine sediment from the Zhuoshui River, north of Mailiao Port in Taiwan, is one of the major sources of sediment supply in this region (Milliman et al. 2007). The annual mean discharge of the Zhuoshui River is approximately 164.8 m^3/s but is up to 24,000 m^3/s during tropical cyclones. Bottle samples collected from bridge stations in the Zhuoshui River during the passage of tropical cyclones suggested that the sediment concentration could exceed 40 g/L for the major duration of the storm (Milliman et al. 2007). Field observations shortly after the passage of a typhoon suggested fine-grained sediments settled rapidly near the river mouth. After Typhoon Morakot in 2009, fine-grained sediment was found in the coastal zone near the river mouth. When this area was resurveyed in 2010, all the fine-grained sediment had been dispersed. It was conjectured that tidal currents and strong wind-driven waves during winter were the mechanisms that transported sediment away from the river mouth (Chien et al. 2011).

A diagnostic study combining field and numerical methods is conducted to improve the understanding of observed morphological evolution in the navigational channel of Mailiao Port. The total area of Mailiao Port is 1,597.7 ha, the interior harbor is 515 ha, the width of harbor opening is 380 m, and the lengths of the navigation channel is approximately 15,000 m (south-wing) and 7,500 m (north-wing). The navigation channel depth is 24 m at the mean-tide level and can accommodate a 300,000-t vessel. Based on the final report of the MHAC (2020), the average daily siltation volume calculated during 2014–2018 was 18,797 m^3/day. Data analysis based on the rate of topographical changes using the empirical orthogonal function (EOF) is discussed in the "Data Analysis using EOF" section. The "Numerical Model" section describes the numerical model for the Yunlin Coast consisting of model description, setup, calibration, and model performance. Results of model simulation are discussed in the "Results and Discussion" section. Finally, "Summary and Conclusions" section concludes the paper.

Data Analysis Using EOF

Lorenz (1956) introduced the EOF which separates the observed variability of bathymetry into independent spatial and temporal modes. The EOF method has been applied to the examination of beach profile variability by several researchers (Aranuvachapun and Johnson 1978; Aubrey 1978; Hsu et al. 1994; Keshtpoor et al. 2013; Lemke and Miller 2017; Ostrowski et al. 1990; Pruszak 1993; Winant et al. 1975). The physical interpretation of the resulting modes can be related to specific physical processes or environmental forces (for example, the littoral drift barrier provided by the breakwaters) which cause the morphological changes (Aubrey 1978). The results of EOF analysis based on the rate of topographical changes were discussed to clarify the hydrodynamic processes which cause observed morphological changes near the navigational channel of Mailiao Port (Huang et al. 2018). The first spatial and temporal EOF components accounted for 63% of the total variation. Fig. 2(a) shows that the first spatial EOF component is closely related to the average rate of topographical changes, as shown in Fig. 1(a). Areas with positive values [Areas A and B in Fig. 2(a)] are related to accretion caused by coastal construction built into the water from the shore that blocks the natural littoral drift. The decreasing trend of the first temporal EOF component describes how the bathymetric changes approach an equilibrium state under the impact of coastal construction [Fig. 3(a)]. The areas with negative values [Area C in Fig. 2(a)] are related to erosion between Sections 26 and 36 [see the location in Figs. 1(a and b)]. To

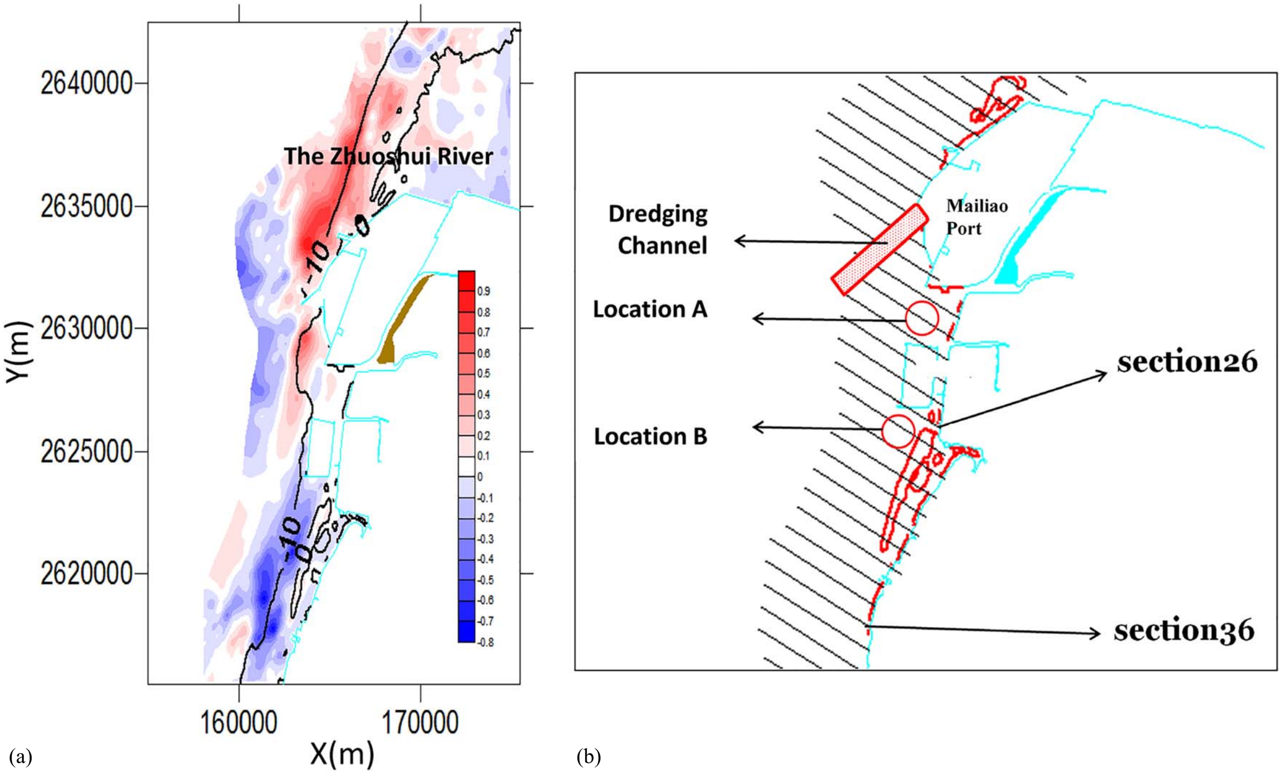

Fig. 1. (Color) (a) Average rate of topographical changes near the mouth of the Zhuoshui River and Mailiao Port (color contours: negative indicates erosion, unit: meter); and (b) location of the dredging channel and sand reclamation (A and B) which cause morphological changes between Section 26 (Taixi) and Section 36 (Santiaolun Fishing Port).

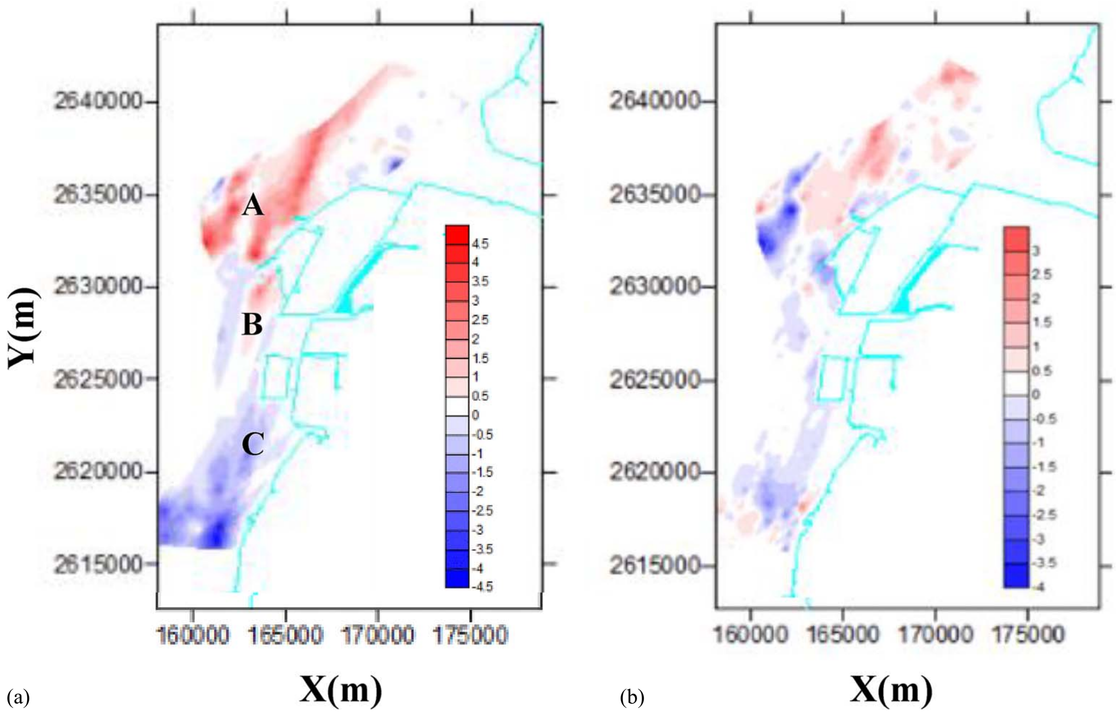

Fig. 2. (Color) Spatial modes of the EOF analysis in the study area: (a) first mode; and (b) second mode. Areas A and B (positive values) in Fig. 2(a) indicate an accretion caused by coastal construction that blocks the natural littoral drift, while area C (negative values) represents an erosion between Sections 26 and 36 mentioned in Fig. 1(b). Fig. 2(b) illustrates an accretion near the river mouth.

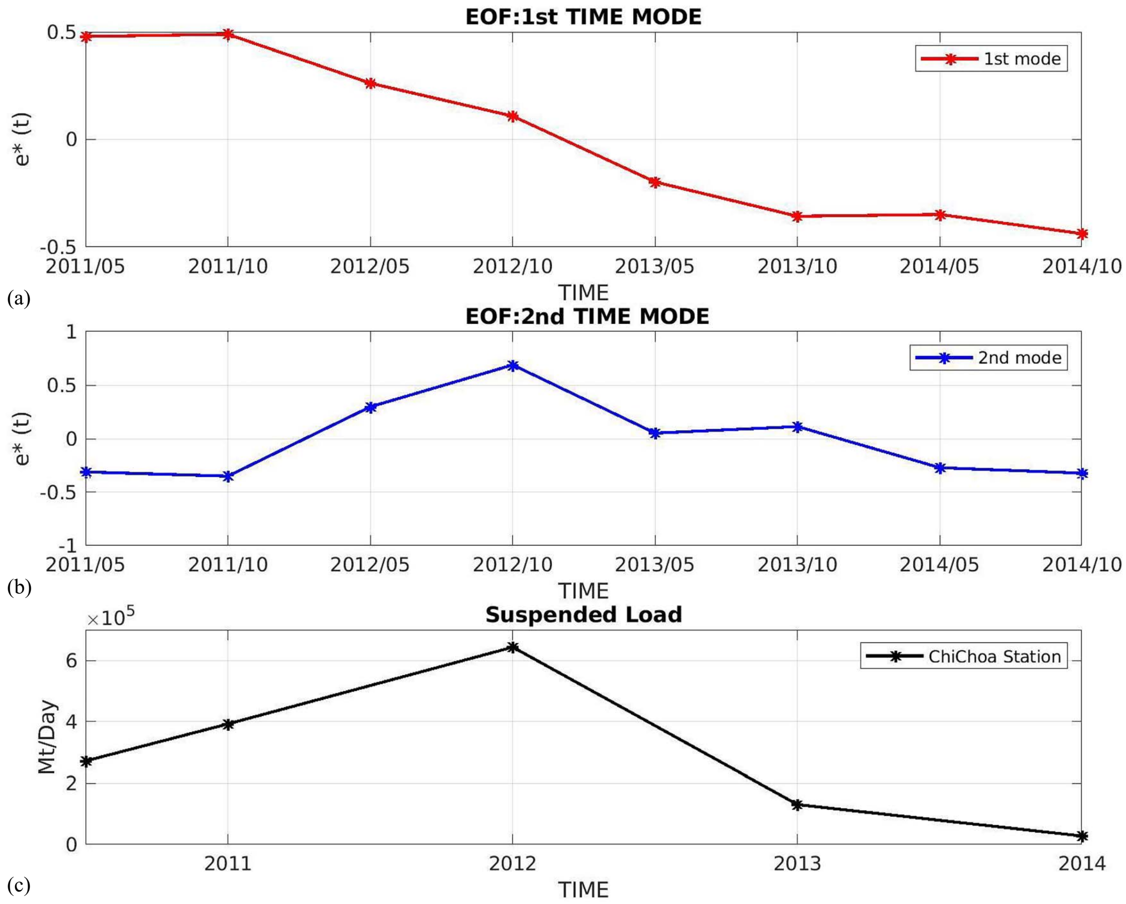

Fig. 3. (Color) Temporal modes of the EOF analysis: (a) first mode; (b) second mode; and (c) the yearly averaged suspended load observed in Xizhou Bridge in the Zhuoshui River.

mitigate the observed seabed erosion, sand reclamation (600,000 m^3 per month) was conducted at two specific locations near the offshore industry park [see the location in Fig. 1(b)]. The second spatial EOF component represents 11% of the total variation, with positive values near the river mouth [Fig. 2(b)]. The temporal distribution of the second mode is correlated with the change in riverine sediment load over the years [Fig. 3(b)], with a correlation coefficient of 64% [based on Eq. (8)]. The peak of the second temporal mode and the observed riverine sediment load turned out in 2012 [Figs. 3(b and c)]. The results of the EOF analysis suggested that the observed morphological changes near the navigation channel are related to the interaction of tides, waves, and coastal construction (63% of the total variation). Therefore, a coupled wave-circulation model is used to provide insights into the patterns of residual circulations and sediment transport for a range of spring-neap tidal forces and wave conditions, improving the understanding of the observed morphological evolution near coastal construction.

Numerical Model

Model Description

Numerical models are widely used by engineers to simulate various aspects of waves, currents, sediment transport, and bathymetric changes in the nearshore ocean and to describe the coastal processes and effects of coastal structures (Bertin et al. 2009; Elias et al. 2006; Keshtpoor et al. 2015; Larson 2005; Malhadas et al. 2009; Pao et al. 2021). NearCoM-TVD 10.0 (Chen et al. 2014; Shi et al. 2011a), a coastal modeling system, integrates the wave model SWAN and a modified version of the circulation model SHORECIRC with sediment transport formulas (Kobayashi et al. 2008; Soulsby 1997; Van Rijn 2011). The numerical model SHORECIRC is a quasi-three–dimensional model that incorporates the mixing effects of vertical structure to a 2D horizontal model for simulating nearshore circulation (Svendsen et al. 2004). Conventional finite-difference schemes often produce unphysical oscillations while modeling coastal processes with abrupt changes or discontinuities, such as tidal bore formation, breaker zones, and moving shorelines. In contrast, a total-variation-diminishing (TVD)-type finite volume, a property of certain discretization schemes used to solve hyperbolic partial differential equations, allows for the robust treatment of discontinuities through the shock-capturing mechanism (Harten 1983). The wave model Simulating Waves Nearshore (SWAN) has been developed (Booij et al. 1999) to estimate wave conditions in small-scale, coastal regions with shallow water, (barrier) islands, tidal flats, local wind, and ambient currents (Ris et al. 1999). This comprehensive model describes a number of nearshore phenomena, such as surf-beat, edge waves, and longshore currents, while allowing for alongshore variations in the hydrodynamic conditions (Dongeren et al. 2016).

Based on the depth integration, the formulations of the SHORECIRC model (Svendsen et al. 2004) in Cartesian coordinates are given as follows:

$$\frac{\partial \eta}{\partial t} + \frac{\partial H u_\alpha}{\partial x_\alpha} = 0 \tag{1}$$

$$\frac{\partial H u_\alpha}{\partial t} + \frac{H u_\alpha u_\beta}{\partial x_\beta} + f_\alpha + gH\frac{\partial \eta}{\partial x_\alpha} + \frac{1}{\rho}\frac{\partial T_{\alpha\beta}}{\partial x_\beta} + \frac{1}{\rho}\frac{\partial S_{\alpha\beta}}{\partial x_\beta} + \frac{\tau_\alpha^b}{\rho} - \frac{\tau_\alpha^s}{\rho} + \mathrm{ROT} = 0 \tag{2}$$

where $H = \eta + h$, η = wave-averaged surface elevation; h = still water level; ρ = density; u_α = component of the short-wave-averaged velocity; and f_α = Coriolis force caused by a deflection of the moving object path within a rotating coordinate system. The parameters $T_{\alpha\beta}$, $S_{\alpha\beta}$, τ_α^b, τ_α^s, and ROT are, respectively, the depth-integrated Reynold's stress, the wave-induced radiation stress (Higgins and Stewart 1962, 1964), the bottom shear stress, the wind-induced surface stress (Church and Thornton 1993), and the rest of terms associated with 3D dispersion.

Waves and currents create bottom shear stress, a force at the seabed that influences sediment texture distribution, microtopography, habitat, and anthropogenic use (Dalyander et al. 2013). The wave-averaged bottom stress equation in the SHORECIRC model (Svendsen and Putrevu 1991) is given as follows:

$$\tau_\alpha^b = \frac{1}{2} f \rho u_0 (\beta_1 u_{b\alpha} + \beta_2 U_{w\alpha}) \tag{3}$$

where $u_{b\alpha}$ = current velocity at the bottom; and u_0 = magnitude of current velocity $u_{b\alpha}$ or the magnitude of wave velocity $U_{w\alpha}$ when $U_{w\alpha} > u_{b\alpha}$. The current velocity, $u_{b\alpha}$, with the weighting factor β_1 and the magnitude of wave velocity, $U_{w\alpha}$, with the weighting factor β_2 are the other contributors to the shear stress τ_α^b. The weighting factors (β_1 and β_2) are the function of $U_{w\alpha}/u_{b\alpha}$ and the angle between wave and current vectors taken from the laboratory experimental data under the monochromatic wave conditions (Svendsen and Putrevu 1991). The values $\beta_1 = 1.0$ and $\beta_2 = 0.5$ (Chen et al. 2014, 2015; Shi et al. 2011a) are used in the present model. The friction factor, f, can be calculated by using the Manning formula, which integrates the effect of water depth, H, into a given Manning coefficient, M (Gauckler 1867; Manning 1891).

$$f = 2gM^2/H^{1/3} \tag{4}$$

Sediment transport and the evolution of seabed in the coastal zone are driven by waves and wave-induced currents. The total sediment transport rate combining the effect of currents and waves on the bed shear stress (Soulsby 1997) is given as follows:

$$q_a = A_s u_a \left[\sqrt{|\boldsymbol{u}|^2 + \frac{0.018}{C_d} u_{\mathrm{rms}}^2} - u^{cr} \right]^{2.4} (1 - 1.6 \tan\beta) \tag{5}$$

where A_s = sediment load; $|\boldsymbol{u}|$ = magnitude of the current velocity; u^{cr} = critical velocity for erosion determined by the water depth and the mean grain size of the sediment (D_{50}); u_{rms} = root mean square of the wave orbital velocity; and β = bed slope. The drag coefficient (C_d) plays an important role in calculating the total sediment transport rate, which is inversely parameterized to the wave stirring and can be defined as follows:

$$C_d = \left[\frac{0.40}{\ln(h/z_0) - 1} \right]^2 \tag{6}$$

The magnitude of wave stirring is also influenced by the bed roughness ($z_o = 0.001$ m). The total load sediment transport model is closely connected to current-dominated conditions in which tidal currents and wave-induced currents determine the direction of net transport, but waves can enhance the magnitude of transport through u_{rms} (Soulsby 1997).

The seabed evolution can be described by using the sediment transport flux in generalized curvilinear coordinates

$$(1 - p)\frac{\partial h_1}{\partial t} + \frac{\partial f_{\mathrm{mor}} q_a}{\partial x_a} = 0 \tag{7}$$

where h_1, p, and f_{mor} = bed evolution, bed porosity, and morphological factor, respectively. Eq. (7) is solved by using an upwinding first-order finite-difference scheme. The dissipation is minimal due to the small-time step used in the circulation model.

(a)

Maps Data: Google Earth / Image © 2021 Maxar Technologies / Image © 2021 TerraMetrics Data SIO, NOAA, U. S. Navy, NGA, GEBCO

(b)

Fig. 4. (Color) (a) Google Earth image of the navigation channel of Mailiao Port (W1: north-wing; W2: south-wing). A red circle indicates the siltation area near the entrance of the port. A, A_m, A', B', B_m, and B are the locations of sediment sample for model simulations. A tidal gauge (T1) and ADCPs (T2, T3, and T4) were deployed in April 2010. In time period 2018–2019, ADCP1 and ADCP2 were deployed at the edge of the navigation channel. MLTS was applied to monitor the tidal level at the entrance of Mailiao Port; and (b) the enlarge view of the Mailiao Port which shows the geometry of the existing North Jetty (700 m), West Jetty, and South Jetty. (Map data © Google Earth/Image © 2021 Maxar Technologies/Image © 2021 Terrametrics, Data SIO, NOAA, U.S. Navy, NGA, GEBCO.)

Model Setup and Calibration

The domain of numerical simulations indicated by the red line box (the length and width of 72 and 19 km, respectively) was rotated 60° clockwise, so the simulated nearshore circulations and sediment fluxes are presented as flowing in the alongshore and cross-shore directions [Figs. 5(a and b)]. The model resolution is 20 m near the Mailiao Port and 200 m in the rest of the domain [Fig. 5(c)]. The tidal boundary condition is provided by the global tidal-level forecast of Oregon State University with eight tidal constituents (K1, O1, P1, Q1, K2, M2, N2, and S2) (Martin et al. 2009). The wave boundary condition is based on the measurements of the offshore wave buoy at the Hsinchu station (25-m water depth). The navigation channel of Mailiao Port consists of two routes to enable the passage of vessels to the port, namely the north wing (W1) and the south wing (W2), and the measurements used for model calibration were taken in several positions as shown in Fig. 4(a). The Mailiao Tides Level Station (MTLS) was applied to monitor the tidal level at the entrance of Mailiao Port. In 2010, a tide gauge and acoustic Doppler current profiler (ADCP) were deployed between the entrance of Mailiao Port and the navigation channel (T1 and T2). ADCPs were deployed at the edge of the ebb tidal delta (T3, 10-m depth) and on the delta of the Zhuoshui River (T4, 6-m depth). Two ADCPs in time period 2018–2019 were deployed to measure the impact of waves and currents near the navigation channel (ADCP1, 400 m from the edge of the navigation channel and ADCP2, 1,000 m from the edge of the navigation channel). These observed time series of surface elevations and current velocities were applied to the model calibration.

The simulations were divided into five cases, as shown in Table 1; Case 1 (30 days), Case 2 (13 days), Case 3 (13 days), Case 4 (10 days), and Case 5 (10 days). In this research, Case 3 and Case 4 were chosen to represent different wave conditions during the winter and summer seasons, respectively. Figs. 6(a and d) show the tidal boundary conditions of Case 3 (October–November 2018) and Case 4 (April 2019). Both the figures show similar results with the high tide levels (1.0–2.0 m) and the low tide levels (−1.0 to −1.2). Figs. 6(b and e) indicate the wave boundary conditions of Case 3 and Case 4 taken from stations of ADCP2 (10-m depth) and ADCP1 (21-m depth) in the offshore area. The highest wave in both cases is around 3.0 m, whereas the lowest wave is around 0.2 m. Wind-driven waves in the period of October–November 2018 (Case 3) were dominantly directed from the north, as shown in the scattered data, whereas the wave direction recorded in April 2019 (Case 4) dominantly came from the south.

Model Performance

Calibration involves the adjustment of model parameters to produce a more reliable simulation (Montanari and Toth 2007). Selecting the appropriate friction parameters [for example, the Manning coefficient in Eq. (4) and the bed roughness z_o in Eq. (6)] in the numerical simulation will determine the success of the modeling calibration. This optimization process for model performance requires several iterative steps by comparing the simulated and observed data. Model calibration was conducted between simulation results and observation data at MTLS for surface elevation and offshore area for tide level, velocity in longshore, and cross-shore direction

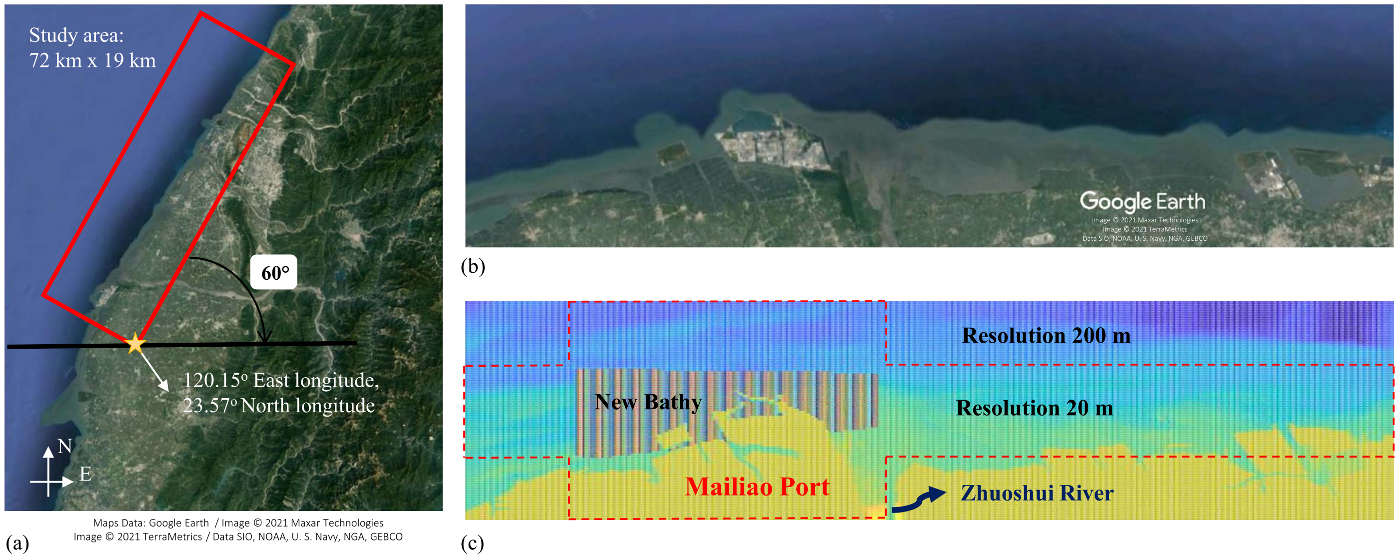

Fig. 5. (Color) (a) Google Earth image of the Yunlin Coast. The red box indicates the study area; (b) Google Earth image of the study area (the map was rotated 60° in clockwise direction); and (c) the computational domain has the finer resolution grid (20 m) near the Mailiao Port and along the coastline, and the coarser resolution (200 m) in the rest of the domain. The digital elevation model (DEM) provided by the Ministry of Science and Technology (MOST), Taiwan, has a 200-m resolution in coastal regions. The new DEM (near the Mailiao Port, re-surveyed in 2018) with a 10-m resolution are indicated by color bars. [Maps in (a and b) images © Google, Image © 2021 Maxar Technologies, Image © 2021 TerraMetrics, Data SIO, NOAA, U.S. Navy, NGA, GEBCO.]

Table 1. Measurement used for model calibration

Case	Station	Water depth (m)	Time
Case 1	T1	9	April 2010
	T2	9	
	T3	13	
	T4	6	
Case 2	ADCP1	21	April 27–May 6, 2018
Case 3	ADCP2	10	October 25–November 16, 2018
Case 4	ADCP1	21	April 1–11, 2019
Case 5	ADCP1	21	May 17–27, 2019
All cases	MLTS	23	All time period

using ADCP. The coherence between the model and measurements was analyzed using the correlation coefficient (R), model skill (S), and the root-mean-square error (RMSE). Considering that M_n and C_n are the measured data and the computed data, respectively, at N discrete points, the formulas are given by

$$R = \frac{(1/N)\sum_{n=1}^{N}(M_n - \overline{M_n})(C_n - \overline{C_n})}{\sigma_C \sigma_M} \quad (8)$$

$$S = 1 - \frac{\sum_{n=1}^{N}|C_n - M_n|^2}{\sum_{n=1}^{N}(|C_n - \overline{M_n}|^2 + |M_n - \overline{M_n}|^2)} \quad (9)$$

$$\text{RMSE} = \left[\frac{1}{N}\sum_{n=1}^{N}(M_n - C_n)^2\right]^{1/2} \quad (10)$$

The correlation coefficient (R) is commonly used to describe the strength of linear association between two quantitative variables, as shown in Eq. (8). Willmott (1981) presented a qualitative calibration method called model skill (S), as shown in Eq. (9). The perfect agreement between the model and observation can be reached if the value of $S = 1$, while the lowest value, $S = 0$, indicates complete disagreement. RMSE can also be used to measure the spread of observed data about the predicted values as shown in Eq. (10), the standard deviation of the residuals. The residuals describe that the distance of data points is from the regression line. RMSE is always between 0 and 1, in which the smaller value presents higher accuracy of the numerical model. For instance, if the distribution of data points lies precisely on the regression line, the RMSE is 0. RMSE is frequently used by researchers due to the easier interpretation results by converting the error metric back into similar units (Chai and Draxler 2014; Neill and Hashemi 2018).

The bottom friction coefficient, Manning's number, of 0.02 is applied to the entire model domain, making bottom friction a function of water depth [Eq. (4)]. In general, the comparison between observed data and simulation results demonstrates that the validated numerical model can simulate the flow field of the study site (Tables 1 and 2). Table 2 demonstrates that the values of the correlation coefficient, model skill, and RMSE for the surface elevation of five cases vary between 0.965–0.983, 0.907–0.971, and 0.232–0.454, respectively. The correlation coefficient for surface elevation shows that model results are strongly correlated with the observations. The model skill for surface elevation also shows a strong model agreement with the observed values. For the comparison of the model and observed velocity, the correlation coefficient for cross-shore velocities (u) varies from 0.934 (Case 2) to 0.159 (Case 3). The correlation coefficient for the longshore current velocities (v) ranges from 0.789 to 0.951, except for T2 (Case 1) which shows $R = -0.002$. The model skill denotes that the velocities in the cross-shore direction vary from 0.177 to 0.921 and the velocities in the longshore direction vary from −0.002 to 0.951. Overall, the correlation coefficient is greater than 0.98 and the model skill is greater than 0.9 for the simulated surface elevation in most of the stations. The correlation coefficient is greater than 0.79, the model skill is greater than 0.71, and the RMSE is less than 0.3 m for the simulated longshore current in most of the stations.

J. Waterway, Port, Coastal, Ocean Eng., 2022, 148(2): 05022001

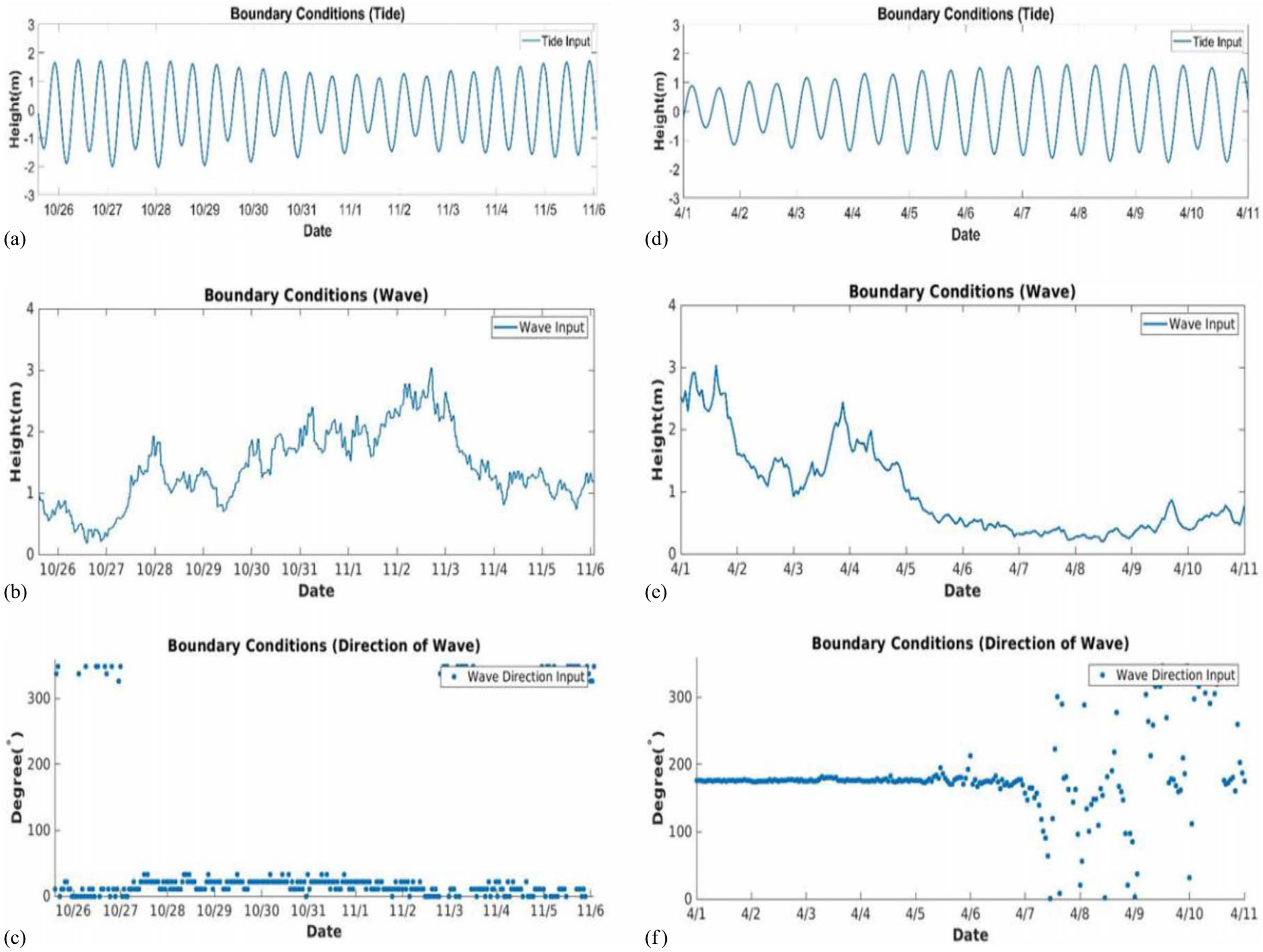

Fig. 6. (Color) (a) Tidal boundary condition; (b) wave boundary condition; (c) wave direction during the winter season measured from October 26 to November 6, 2018 (Case 3); the wave direction around 30° shows the actual wave direction based on the degree of the compass (i.e., 0 in North); (d) tidal boundary condition; (e) wave boundary condition; and (f) wave direction during the summer season measured from April 1 to 11, 2019 (Case 4). The actual wave direction comes from 180°.

Table 2. Model performance of the five model simulations

		Correlation coefficient (R)			Model performance (S)			RMSE		
Case	Station	η	u	v	η	u	v	η	u	v
Case 1	MLTS	0.978	—	—	0.962	—	—	0.238	—	—
	T1	0.965	—	—	0.948	—	—	0.278	—	—
	T2	0.983	0.379	−0.002	0.960	0.177	−0.002	0.246	0.423	0.047
	T3	—	0.787	0.789	—	0.829	0.781	—	0.102	0.322
	T4	—	0.807	0.801	—	0.751	0.710	—	0.193	0.280
Case 2	MTLS	0.966	—	—	0.907	—	—	0.454	—	—
	ADCP1	0.970	0.934	0.951	0.962	0.921	0.951	0.267	0.077	0.119
Case 3	MTLS	0.979	—	—	0.932	—	—	0.393	—	—
	ADCP2	0.973	0.159	0.796	0.967	0.091	0.794	0.245	0.085	0.314
Case 4	MTLS	0.975	—	—	0.965	—	—	0.249	—	—
	ADCP1	0.980	0.810	0.951	0.963	0.395	0.928	0.252	0.139	0.161
Case 5	MTLS	0.973	—	—	0.962	—	—	0.259	—	—
	ADCP1	0.978	0.790	0.831	0.971	0.723	0.796	0.232	0.126	0.212

Fig. 7 compares the modeled results and observed surface elevation and velocities from ADCP2 for Case 3 and ADCP1 for Case 4. The simulated surface elevation of Case 3 [Fig. 7(a), the RMSE is 0.245 and the NRMSE is 17.5%] indicates an underestimate from the observed data during flood tides. NRMSE is a normalized RMSE obtained by dividing the RMSE value with the mean of tidal amplitudes. During ebb tides, the model results almost coincide with the observed surface elevation. The

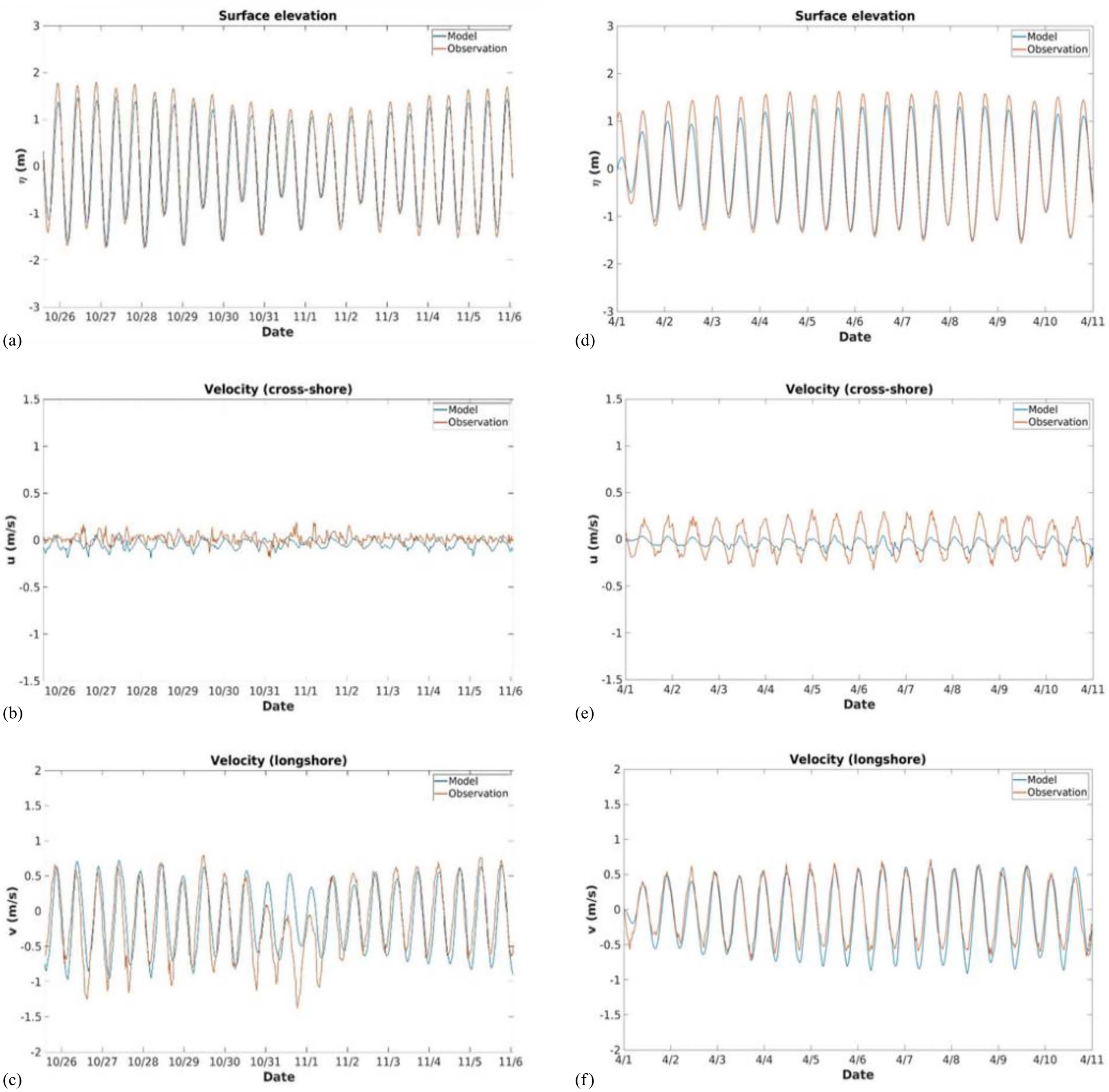

Fig. 7. (Color) Comparisons of modeled results (blue curves) and ADCP2 (10-m depth, Case 3): (a) surface elevation; (b) cross-shore velocity; (c) alongshore velocity; the comparisons of modeled results and measurements at ADCP1 (21-m depth, Case 4); (d) surface elevation; (e) cross-shore velocity; and (f) alongshore velocity.

comparison of the tidal surface elevation for Case 4 shows a similar trend as Case 3, in which the observed tidal range is larger than the simulated results (the RMSE is 0.252 and the NRMSE is 16.8%). The velocity in the longshore direction of Case 3 shows that the modeled results are in a similar trend as the observational data, except for greater values in longshore velocities from October 30 to November 1, 2018 [Fig. 7(c)], most likely due to the influence of Typhoon Yutu. The comparison between the model results and observations in Case 4 demonstrates that the modeled longshore currents fit the observation during flood tides, whereas modeled longshore currents are greater than the observations during ebb [Fig. 7(f)]. The modeled results of cross-shore currents are underestimated compared with the observation in ADCP1 (21-m depth, near the navigation channel) as shown in Fig. 7(e), possibly owing to the change in the main direction of tidal currents change near the navigation channel over the abrupt depth that was not captured by the model bathymetry with a resolution of 20 m.

Results and Discussion

Seasonal Variations in Significant Wave Heights and Directions

The simulated wave and flow field during two representative conditions, the northeastern monsoon during the winter season

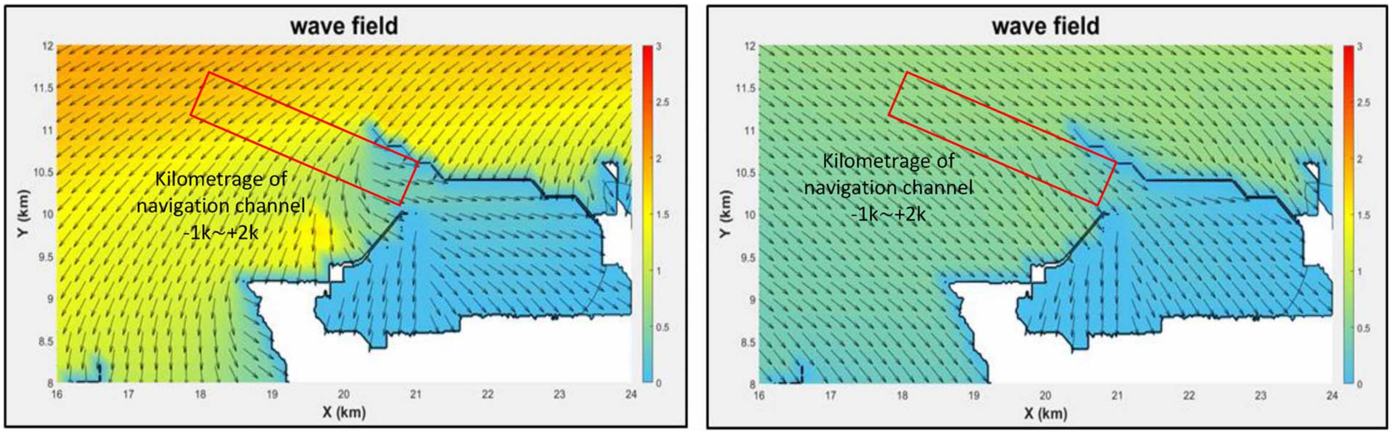

(a)

(b)

Fig. 8. (Color) Modeled results of significant wave heights and direction of (a) Case 3; and (b) Case 4. A red box indicates the location of the navigation channel.

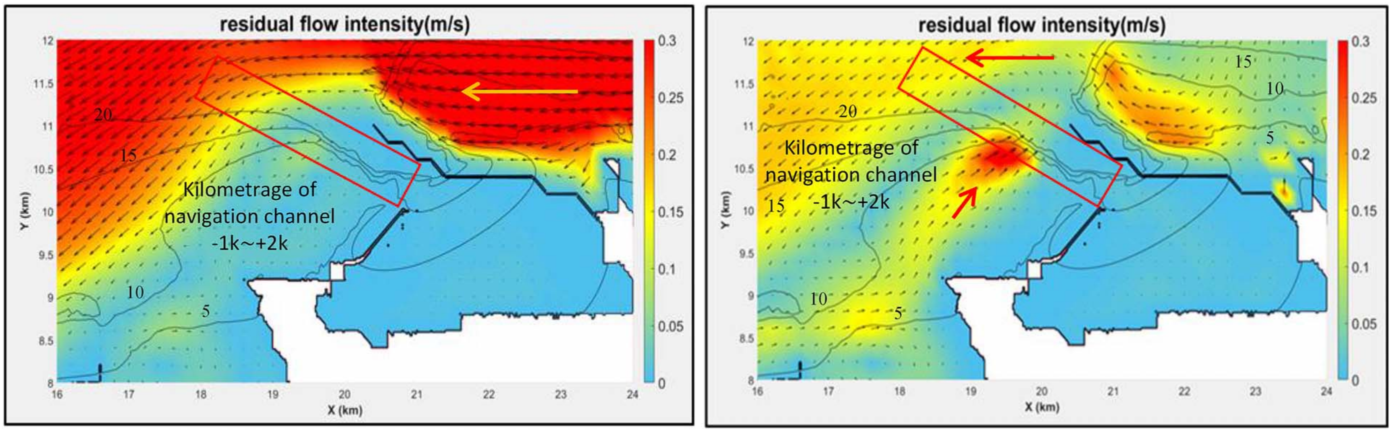

(a)

(b)

Fig. 9. (Color) Modeled results of residual flow intensity of (a) Case 3; and (b) Case 4. A red box indicates the location of the navigation channel.

(Case 3, November 2–3, 2018) and the southern wind condition during the summer season (Case 4, April 1–2, 2018), are discussed in this section. The simulated flow field in Case 1, Case 2, and Case 5 are mainly dominated by tides due to weaker wave energy during the spring and summer seasons (the significant wave heights observed by the offshore data buoy are generally less than 1 m). Fig. 8 shows the magnitude and the direction of simulated significant wave heights in the study area during the winter and summer season [see the wave heights and direction in Figs. 6(b, c, e, and f)]. During the winter season when the magnitude of offshore waves is approximately 2.5 m, the simulated significant wave heights near the port are approximately 1 m and predominantly from the northwest toward the east. The observed wave heights and directions in Figs. 6(e and f) show that the wave direction during the summer season is from the south to the north with relatively milder wave energy than that in the winter season. During the summer season when the magnitude of offshore waves is approximately 1.5 m, the magnitude of significant wave heights is approximately 0.5 m near the port and waves propagate directly toward the entrance of the port. The simulated flow field under the interaction of waves and tidal currents during two representative conditions, namely the northeastern monsoon during the winter season and the southern wind condition during the summer season, are further discussed in the subsequent section.

Seasonal Variations in Residual Circulations

Tidal currents produce variations in the flow fields at different tidal stages. Both the modeled and observed current velocities (Fig. 7) show that the velocity in the longshore direction is more dominant. The velocity in the cross-shore direction is small and random [see the example in Case 3, Fig. 7(b)]. The average discharge of Case 3 is 24.95 m^3/s and the average discharge of Case 4 is 11.73 m^3/s. The velocities of the riverine flow are negligible when compared with the annual mean discharge of the Zhuoshui River ($\sim$164.8 m^3/s) and the discharge during tropical cyclones as well. Therefore, the effect of the riverine flow on current velocities near the navigational channel and the port entrance is insignificant compared with tidal currents or wave-driven longshore currents. The model results show that the tidal currents move toward the south during ebb tides, and the tidal currents move toward the north during flood tides. A striking difference between the intensity of residual circulations in Case 3 and Case 4 is shown in Fig. 9 (the tidal amplitude is approximately 0.5 m which are similar in both cases). The residual circulations refer to the flow integrated over

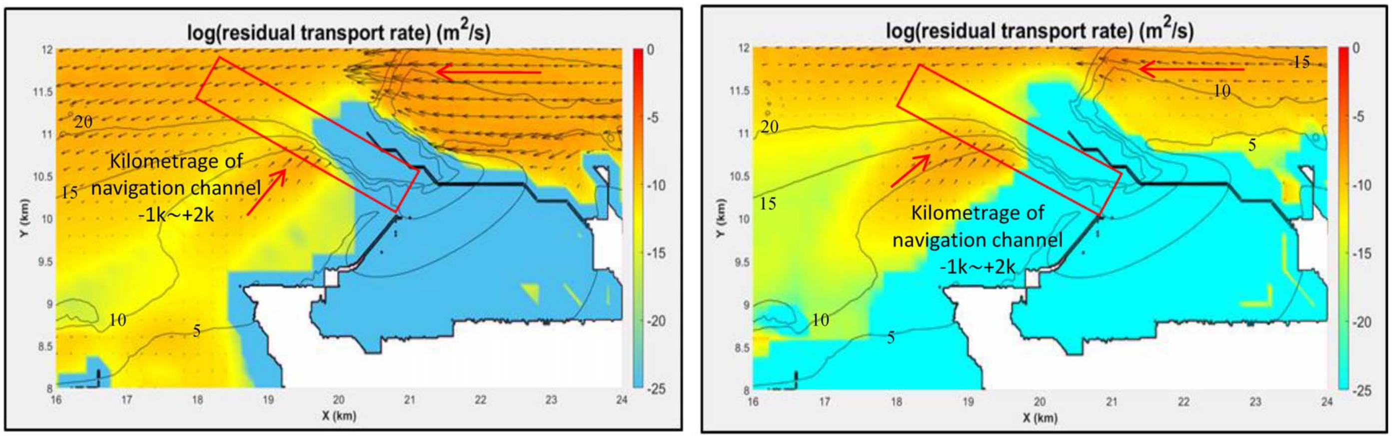

(a)

(b)

Fig. 10. (Color) Modeled results of residual transport rate of (a) Case 3; and (b) Case 4. A red box indicates the navigation channel and the arrows denote the direction of sediment flux.

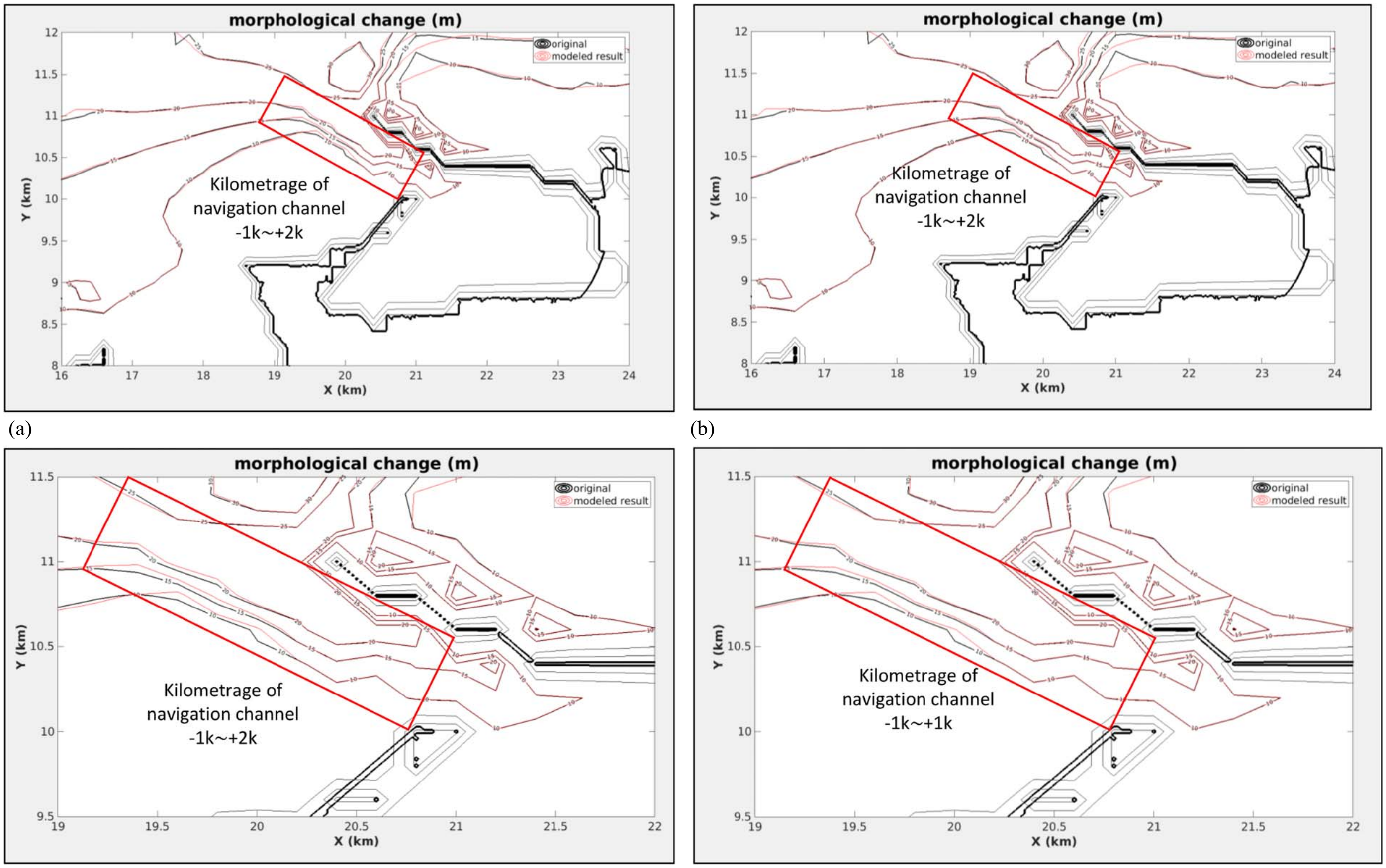

(a)

(b)

(c)

(d)

Fig. 11. (Color) Morphological changes of (a) Case 3; (b) Case 4; and (c and d) enlarged view of morphological changes in Case 3 and Case 4.

one tidal period defined by the dominant constituent [for example, the period of M2 is 12.74 h; see Eq. (11)].

$$u_{\text{residual}} = \frac{1}{12.74} \sum_{i=1}^{12.74} u_i \tag{11}$$

Therefore, residual circulations can be used to estimate the direction and the intensity of the net sediment transport which possibly causes siltation or erosion near the navigation channel of Mailiao Port. In Case 3, the residual flow moves from the north toward the south. The port basin and the navigational channel near the port entrance are relatively stable without disturbances induced by tides and waves. The location of 2 km from the port entrance is influenced by the residual circulations with a speed up to 0.3 m/s from the north [see the yellow arrow in Fig. 9(a)]. In Case 4, the magnitude of residual circulations decreases during the summer season. The location of 2 km from the port entrance is influenced by the residual circulation with the speed of approximately

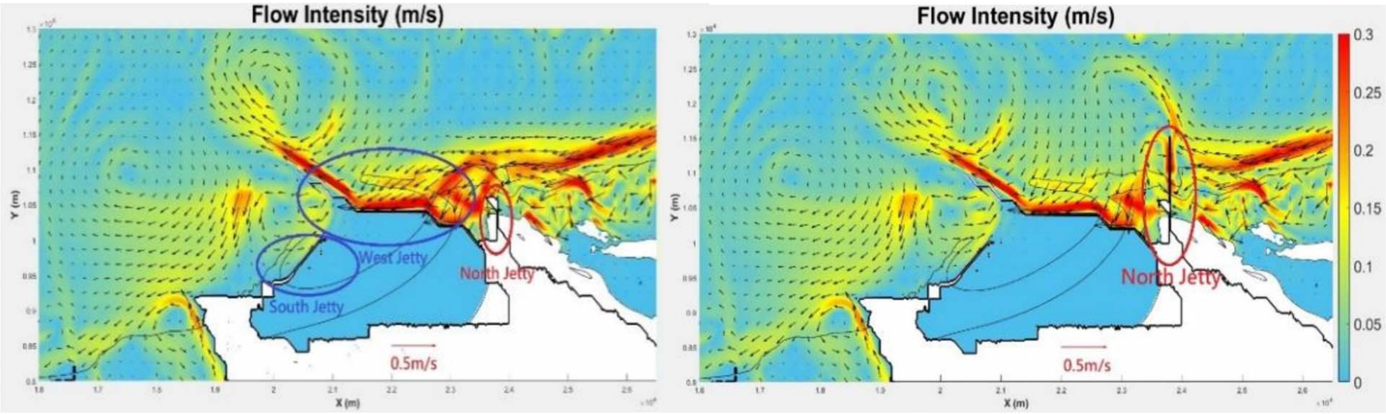

(a)

(b)

Fig. 12. (Color) Simulated flow intensity of wave-induced longshore current near the navigational channel of Mailiao Port: (a) simulated flow intensity near the navigational channel with the existing North Jetty (700 m, shown in the red circle); and (b) simulated flow intensity near the navigational channel with the extended North Jetty (1,700 m).

0.15 m/s originally coming from the north toward the south. The northward transport is enhanced with the additional flow coming from the south with a speed of 0.2–0.3 m/s occurring near the port entrance in the navigational channel [see the red arrow from both the north and south in Fig. 9(b)]. The model results for residual circulations under different wave conditions demonstrate that the magnitude and the direction of the simulated residual circulations near the edge of the navigation channel are modulated by offshore wave conditions.

Simulated Morphological Change and a Countermeasure to Reduce Siltation

The simulated residual sediment flux and the resulting morphological evolution during two representative conditions are further discussed based on the total load transport formula of Soulsby (1997). D_{50} is given as 0.1 mm according to the sample from the field experiment [see the location in Fig. 4(a)]**.** The critical shear stress for erosion defined by Van Rijn (1984) varies between 0.39 and 0.45 m/s at a water depth of 5–30 m based on the given D_{50}. Therefore, the sediment transport near the navigation channel can be triggered by the relatively strong current velocities [ranging between 0.5 and 1.0 m/s, see the example of observed and modeled velocities in the longshore direction in Figs. 7(c and f)]. Similar to the pattern of the simulated residual circulations, the simulated residual sediment transport rate at the location of 2 km from the port entrance is influenced by tides and wave-induced currents from the north. The simulated sediment transport rates for Case 3 and Case 4 come from the south toward the navigation channel and the entrance of the port (indicated by red vectors in Fig. 10). Moreover, the black and red contours in Fig. 11 illustrate the model results of morphological change after 1 month of simulation with a morphological factor of 12 which implies a 12-month multiplier to the sediment continuity equation. The simulated morphological evolution displays changes in the depth along the navigation channel during both seasons. The seabed change location is consistent with the spot indicated by the red circle in Fig. 4(a).

The model results indicate that tidal currents play an important role in net transport southward, and wave-driven longshore currents may further transport the sediments from the riverine deposition near the mouth. The model results also indicate that the magnitude of sediment transport rate is more persistent under the northeast monsoon condition during the winter season. The magnitude and direction of wave-induced longshore current along the Yunlin Coast during the typical winter season are illustrated in Fig. 12(a). The wave-induced longshore currents (~0.3 m/s) may contribute to 30%–60% of the total flow intensity under the interaction of tides and waves [0.5–1.0 m/s; Fig. 7(c)].

The Mailiao Port has three existing jetties which are the North, West, and South Jetty [shown in Fig. 4(b)]. The length of the existing North Jetty is 700 m. Model simulation demonstrates that the longshore current interacts with the South Jetty and forms a circulation pattern that may transport sediment material into the navigational channel and causing the morphological evolution [Figs. 11(c and d)]. It is suspected that the North Jetty is incapable of blocking the supply of sediment transport from the deposited riverine sediment near the river mouth because the simulated morphological change is also significant near the West Jetty [Figs. 11(a and b)]. A striking difference can be seen when the North Jetty is extended to a water depth of 22 m (similar to the West Jetty). The extension of the North Jetty (1,700 m) redirects the transport of longshore currents from the river mouth by modifying the circulation system. If the longshore current is blocked, the direction current changes toward the West, as shown in Fig. 12(b). The model results suggest that the extension of the North Jetty could be a countermeasure to reduce the siltation by modifying the circulation system between the port and the river mouth.

Summary and Conclusions

The observed data used in this research were from fixed oceanographic stations in different periods, including surface elevations, current velocities, bathymetry, and other significant data to obtain the time series of hydrodynamic and sediment transport conditions. Analyses of morphological changes using the EOF method, which separate the observed variability of bathymetry into independent spatial and temporal modes, suggest that the first mode (63%) is relevant to the construction of the coastal structure and the second mode (11%) is relevant to riverine sediment. The second mode based on EOF analysis indicates that the riverine sediment contributes to the morphological changes near the river mouth in the northern part of the port. It is suspected that wave-induced longshore currents—dominantly from the north toward the south—further transport sediment deposition in the northern part of the port to the navigation channel or the port basin. To understand the potential cause for the observed morphological change suggested by EOF analysis, a numerical model is presented to investigate the patterns of residual circulations and sediment transport for a range of spring-neap tidal forces and wave conditions over the complex bathymetry. NearCom-TVD is used to simulate the interaction between tides, waves, and longshore currents in response to siltation occurring in the navigation channel. The model results suggest that tidal currents play an important role in net transport southward, and wave-driven longshore currents also transport a significant amount of sediment from the river mouth during the northeastern monsoon season. The wave direction during the summer season is from the south toward the north with relatively milder wave energy when compared with that in the winter season. The wave-induced longshore current during the typical winter season contributes to 30%–60% of the flow intensity. The model results suggest that the extension of North Jetty could be one of the engineering means to modify the circulation system between the port and the river mouth to mitigate the siltation problem.

Data Availability Statement

The program for EOF analysis and the source code of the NearCoM-TVD used during the study are available from the corresponding author by request.

Acknowledgments

Funding was provided by Taiwan’s Ministry of Science and Technology (Grant Nos. MOST 109-2621-M-008-005 and MOST 110-2611-M-006-003), and the funding for conducting bathymetric survey was supported by Yunlin Offshore Industrial Park Service Center. Dr. Nobu Kobayashi is gratefully acknowledged for providing suggestions. Simulations were carried out on the MobyDick at the National Cheng Kung University. Computer resources, technical expertise, and assistance provided by the MobyDick staff are gratefully acknowledged. The authors would also like to thank Harley Winer, Ph.D., P.E. and two anonymous reviewers for detailed feedback that contributed to the improvement of this manuscript.

Notation

The following symbols are used in this paper:

A_s = sediment load;
C_d = drag coefficient;
C_n = computed data;
$\overline{C_n}$ = average-computed data;
f = constant friction factor;
f_{mor} = morphological factor;
f_α = Coriolis force caused by a deflection of the moving object path within a rotating coordinate system;
g = acceleration of gravity;
H = water depth calculated from $(\eta + h)$, in which h is still water level;
h_1 = bed evolution;
M = Manning coefficient;
M_n = measured data;
$\overline{M_n}$ = average-measured data;
N = discrete points;
p = bed porosity;
q_α = total sediment transport rate;
ROT = rest associated with 3D dispersion;
$S_{\alpha\beta}$ = wave-induced radiation stress;
$T_{\alpha\beta}$ = depth-integrated Reynold stress;
$U_{w\alpha}$ = magnitude of wave velocity;
u = velocity in cross-shore direction;
$|\boldsymbol{u}|$ = magnitude of the current velocity;
u_0 = magnitude of the current velocity ($u_{b\alpha}$) or magnitude of wave velocity $U_{w\alpha}$ when $U_{w\alpha} > u_{b\alpha}$;
u^{cr} = threshold velocity of sediment motion given by Van Rijn (1984);
$u_{b\alpha}$ = current velocity at the bottom;
u_{rms} = root-mean-square wave orbital velocity;
u_α = component of the short-wave-averaged velocity;
v = velocity in longshore direction;
z_o = bed roughness;
η = wave-averaged surface elevation;
ρ = density;
τ_α^b = bottom shear stress;
τ_α^s = wind-induced surface stress;
β = bed slope;
σ_C = standard deviation of observation; and
σ_M = standard deviation of the model.

References

Aranuvachapun, S., and J. A. Johnson. 1978. “Beach profile at Gorleston and Great Yarmouth.” *Coastal Eng.* 2: 201–213. https://doi.org/10.1016/0378-3839(78)90020-0.

Aubrey, D. G. 1978. “Statistical and dynamical prediction of changes of natural sand beaches.” Ph.D. thesis, Scripps Institution of Oceanography, Univ. of California.

Bertin, X., A. B. Fortunato, and A. Oliveira. 2009. “A modeling-based analysis of processes driving wave-dominated inlets.” *Cont. Shelf Res.* 29 (5–6): 819–834. https://doi.org/doi.org/10.1016/j.csr.2008.12.019.

Booij, N., R. C. Ris, and L. H. Holthuijsen. 1999. “A third-generation wave model for coastal regions 1. Model description and validation.” *J. Geophys. Res.* 104 (C4): 7649–7666. https://doi.org/10.1029/98JC02622.

Chai, T., and R. R. Draxler. 2014. “Root mean square error (RMSE) or mean absolute error (MAE)?—Arguments against avoiding RMSE in the literature” *Geosci. Model Dev.* 7 (3): 1247–1250. https://doi.org/10.5194/gmd-7-1247-2014.

Chen, J.-L., T.-J. Hsu, F. Shi, B. Raubenheimer, and S. Elgar. 2015. “Hydrodynamic and sediment transport modeling of New River Inlet (NC) under the interaction of tides and waves.” *J. Geophys. Res.* 120 (6): 4028–4047. https://doi.org/doi.org/10.1002/2014JC010425.

Chen, J.-L., F. Shi, T.-J. Hsu, and J. T. Kirby. 2014. “NearCom-TVD—A quasi-3D nearshore circulation and sediment transport model.” *Coastal Eng.* 91: 200–212. https://doi.org/doi.org/10.1016/j.coastaleng.2014.06.002.

Chien, H., W.-S. Chiang, S.-J. Kao, J. T. Liu, K.-K. Liu, and P. L.-F. Liu. 2011. “Sediment dynamics observed in the Jhoushuei River and adjacent coastal zone in Taiwan Strait.” *Oceanography* 24 (4): 122–131. https://doi.org/10.5670/oceanog.2011.100.

Church, J. C., and E. B. Thornton. 1993. “Effects of breaking wave induced turbulence within a longshore current model.” *Coastal Eng.* 20 (1–2): 1–28. https://doi.org/10.1016/0378-3839(93)90053-B.

Dalyander, P. S., B. Butman, C. R. Sherwood, R. P. Signell, and J. L. Wilkin. 2013. “Characterizing wave- and current-induced bottom shear stress: US middle Atlantic continental shelf.” *Cont. Shelf Res.* 52: 73–86. https://doi.org/10.1016/j.csr.2012.10.012.

Dongeren, A. R. V., F. E. Sancho, I. A. Svendsen, and U. Putrevu. 2016. “SHORECIRC: A quasi 3D nearshore model.” In Vol. 3 of *Proc., from the 24th Int. Conf. on Coastal Engineering*, edited by B. L. Edge, 2741–2754. Reston, VA: ASCE.

Elias, E. P. L., J. Cleveringa, M. C. Buijsman, J. A. Roelvink, and M. J. F. Stive. 2006. “Field and model data analysis of sand transport patterns in

Texel Tidal inlet (the Netherlands).” *Coastal Eng.* 53 (5–6): 505–529. https://doi.org/10.1016/j.coastaleng.2005.11.006.

Gauckler, P. 1867. *Études théoriques et pratiques sur l’écoulement et le mouvement des eaux*. Paris: Gauthier-Villars.

Harten, A. 1983. “High resolution schemes for hyperbolic conservation laws.” *J. Comput. Phys.* 49 (3): 357–393. https://doi.org/10.1016/0021-9991(83)90136-5.

Higgins, M. S. L., and R. W. Stewart. 1962. “Radiation stress and mass transport in gravity waves, with application to ‘surf beats’” *J. Fluid Mech.* 13 (4): 481–504. https://doi.org/10.1017/S0022112062000877.

Higgins, M. S. L., and R. W. Stewart. 1964. “Radiation stresses in water waves; a physical discussion, with applications.” *Deep Sea Res. Oceanogr. Abstr.* 11 (4): 529–562. https://doi.org/10.1016/0011-7471(64)90001-4.

Hsu, T.-W., S.-H. Ou, and S.-K. Wang. 1994. “On the prediction of beach changes by a new 2D empirical eigenfunction model.” *Coastal Eng.* 23 (3–4): 255–270. https://doi.org/10.1016/0378-3839(94)90005-1.

Huang, Y.-Q., J.-H. Lin, R.-Y. Yang, Y.-Y. Chen, and J.-L. J. Chen. 2018. “Beach response to exposed riverine sediment and beach nourishment.” *Coastal Eng. Proc.* 1 (36): 92. https://doi.org/10.9753/icce.v36.sediment.92.

Jan, S., J. Wang, C.-S. Chern, and S.-Y. Chao. 2002. “Seasonal variation of the circulation in the Taiwan Strait.” *J. Mar. Syst.* 35 (3–4): 249–268. https://doi.org/doi.org/10.1016/S0924-7963(02)00130-6.

Johannesson, L. T., R. L. Stevens, and J. H. Alexanderson. 2000. “Sediment character in a micro-tidal, harbor-estuary environment, Göteborg, Sweden.” *Estuaries* 23 (3): 400–410. https://doi.org/10.2307/1353332.

Keshtpoor, M., J. A. Puleo, J. Gebert, and N. G. Plant. 2013. “Beach response to a fixed sand bypassing system.” *Coastal Eng.* 73: 28–42. https://doi.org/10.1016/j.coastaleng.2012.09.006.

Keshtpoor, M., J. A. Puleo, F. Shi, and N. R. DiCosmo. 2015. “Numerical simulation of nearshore hydrodynamics and sediment transport downdrift of a tidal inlet.” *J. Waterway, Port, Coastal, Ocean Eng.* 141 (2): 04014035. https://doi.org/10.1061/(ASCE)WW.1943-5460.0000273.

Kobayashi, N., A. Payo, and L. Schmied. 2008. “Cross-shore suspended sand and bed load transport on beaches.” *J. Geophys. Res.* 113 (C7): C07001. https://doi.org/doi.org/10.1029/2007JC004203.

Larson, M. 2005. “Numerical modeling.” In *Encyclopedia of coastal science*, edited by M. L. Schwartz, 730–733. Dordrecht, Netherlands: Springer. https://doi.org/10.1007/1-4020-3880-1_232.

Lemke, L., and J. K. Miller. 2017. “EOF analysis of shoreline and beach slope variability at a feeder beach constructed within a groin field at Long Branch, New Jersey.” *Coastal Eng.* 121: 14–25. https://doi.org/10.1016/j.coastaleng.2016.11.001.

Li, Y., Z. Song, G. Peng, X. Fang, P. Chen, and H. Hong. 2019. “Modeling hydro-dynamics in a harbor area in the Daishan Island, China.” *Water* 11 (2): 192. https://doi.org/10.3390/w11020192.

Lorenz, E. N. 1956. *Empirical orthogonal functions and statistical weather prediction*, 1–49. Cambridge, MA: Massachusetts Institute of Technology Dept. of Meteorology.

MHAC (Mailiao Harbor Administration Corporation). 2020. *Research on drifting sand and siltation in mailiao port channel and preventive measures (Chinese version)*. Final Rep. Taiwan: MHAC.

Malhadas, M. S., P. C. Leitão, A. Silva, and R. Neves. 2009. “Effect of coastal waves on sea level in Óbidos Lagoon, Portugal.” *Cont. Shelf Res.* 29 (9): 1240–1250. https://doi.org/doi.org/10.1016/j.csr.2009.02.007.

Manning, R. 1891. “On the flow of water in open channels and pipes.” *Trans. Inst. Civ. Eng. Ireland* 20: 161–207.

Martin, P. J., S. Smith, P. G. Posey, and G. M. Dawson. 2009. *Use of the Oregon State University Tidal Inversion Software (OTIS) to generate improved tidal prediction in the East-Asian Seas*. Hancock County, MS: Naval Research Laboratory, Oceanography Division, Stennis Space Center.

Milliman, J. D., S. W. Lin, S. J. Kao, J. P. Liu, C. S. Liu, J. K. Chiu, and Y. C. Lin. 2007. “Short-term changes in seafloor character due to flood-derived hyperpycnal discharge: Typhoon Mindulle, Taiwan, July 2004.” *Geology* 35 (9): 779–782. https://doi.org/10.1130/G23760A.1.

Montanari, A., and E. Toth. 2007. “Calibration of hydrological models in the spectral domain: An opportunity for scarcely gauged basins?” *Water Resour. Res.* 43 (5): W05434. https://doi.org/10.1029/2006WR005184.

Neill, S. P., and M. R. Hashemi. 2018. *Fundamentals of ocean renewable energy*. London: Academic Press.

Nijs, M. A. J. D., J. C. Winterwerp, and J. D. Pietrzak. 2009. “On harbour siltation in the fresh-salt water mixing region.” *Cont. Shelf Res.* 29 (1): 175–193. https://doi.org/10.1016/j.csr.2008.01.019.

Ostrowski, R., Z. Pruszak, and R. B. Zeidler. 1990. “Multi-scale nearshore and beach and changes.” In *Coastal Engineering 1990*, edited by B. L. Edge, 2101–2116. Reston, VA: ASCE.

Pao, C.-H., J.-L. Chen, S.-F. Su, Y.-C. Huang, W.-H. Huang, and C.-H. Kuo. 2021. “The effect of wave-induced current and coastal structure on sediment transport at the Zengwen River Mouth.” *J. Mar. Sci. Eng.* 9 (3): 333. https://doi.org/10.3390/jmse9030333.

Prumm, M., and G. Iglesias. 2016. “Impacts of port development on estuarine morphodynamics: Ribadeo (Spain).” *Ocean Coastal Manage.* 130: 58–72. https://doi.org/10.1016/j.ocecoaman.2016.05.003.

Pruszak, Z. 1993. “The analysis of beach profile changes using Dean’s method and empirical orthogonal functions.” *Coastal Eng.* 19 (3–4): 245–261. https://doi.org/10.1016/0378-3839(93)90031-3.

Ris, R. C., L. H. Holthuijsen, and N. Booij. 1999. “A third-generation wave model for coastal regions: 2. Verification.” *J. Geophys. Res.* 104 (C4): 7667–7681. https://doi.org/10.1029/1998JC900123.

Schijndel, S. A. H., and C. Kranenburg. 1998. “Reducing the siltation of a river harbour.” *J. Hydraul. Res.* 36 (5): 803–814. https://doi.org/10.1080/00221689809498604.

Shi, F., D. M. Hanes, J. T. Kirby, L. Erikson, P. Barnard, and J. Eshleman. 2011a. “Pressure-gradient-driven nearshore circulation on a beach influenced by a large inlet-tidal shoal system.” *J. Geophys. Res.* 116 (C4): C04020. https://doi.org/10.1029/2010JC006788.

Soulsby, R. 1997. *Dynamics of marine sands*. London: ICE Publishing.

Svendsen, I. A., K. Haas, and Q. Zhao. 2004. *Quasi-3D nearshore circulation model SHORECIRC version 2.0*. Newark, DE: Center for Applied Coastal Research, Univ. of Delaware.

Svendsen, I. A., and U. Putrevu. 1991. “Nearshore circulation with 3-D profiles.” In *Proc., 22nd Conf. on Coastal Engineering*, edited by B. L. Edge, 241–254. Reston, VA: ASCE.

Van Rijn, L. C. 1984. “Sediment transport, Part III: Bed forms and alluvial roughness.” *J. Hydraul. Eng.* 110 (12): 1733–1754. https://doi.org/10.1061/(ASCE)0733-9429(1984)110:12(1733).

Van Rijn, L. C. 2011. *Principles of fluid flow and surface waves in rivers, estuaries, seas, and oceans*. Delft, Netherlands: Aqua Publications.

Willmott, C. J. 1981. “On the validation of models.” *Phys. Geogr.* 2 (2): 184–194. https://doi.org/10.1080/02723646.1981.10642213.

Winant, C. D., D. L. Inman, and C. E. Nordstorm. 1975. “Description of seasonal beach changes using empirical eigenfunctions.” *J. Geophys. Res.* 80 (15): 1979–1986. https://doi.org/10.1029/JC080i015p01979.

Xiao, Z., X. H. Wang, M. Roughan, and D. Harrison. 2019. “Numerical modelling of the Sydney Harbour Estuary, New South Wales: Lateral circulation and asymmetric vertical mixing.” *Estuarine Coastal Shelf Sci.* 217: 132–147. https://doi.org/10.1016/j.ecss.2018.11.004.

Yu, H., H. Yu, L. Wang, L. Kuang, H. Wang, Y. Ding, S. Ito, and J. Lawen. 2017. “Tidal propagation and dissipation in the Taiwan Strait.” *Cont. Shelf Res.* 136: 57–73. https://doi.org/10.1016/j.csr.2016.12.006.